Direct Z-scheme Heterojunction of $CsPbBr_3/SnS_2$ Nanosheets for Visible Light-Driven Photocatalytic CO_2 Reduction

Li-Yuan Wu,[a] Fei Zhang,[a] Ming-zhe Cai,[a] Min Zhang,[b] Tong-Bu Lu,[b] Ping Li*[c] and Yong-Hua Chen*[a,c]

[a] Henan Institute of Flexible Electronics (HIFE) and School of Flexible Electronics (SoFE), Henan University, 379 Mingli Road, Zhengzhou 450046, China

[b] MOE International Joint Laboratory of Materials Microstructure, Institute for New Energy Materials and Low Carbon Technologies, School of Materials Science and Engineering, Tianjin University of Technology, Tianjin 300384, China.

[c] State Key Laboratory of Flexible Electronics (LoFE) & Institution of Advanced Materials (IAM), School of Flexible Electronics (Future Technologies), Nanjing Tech University, Nanjing 211816, China.

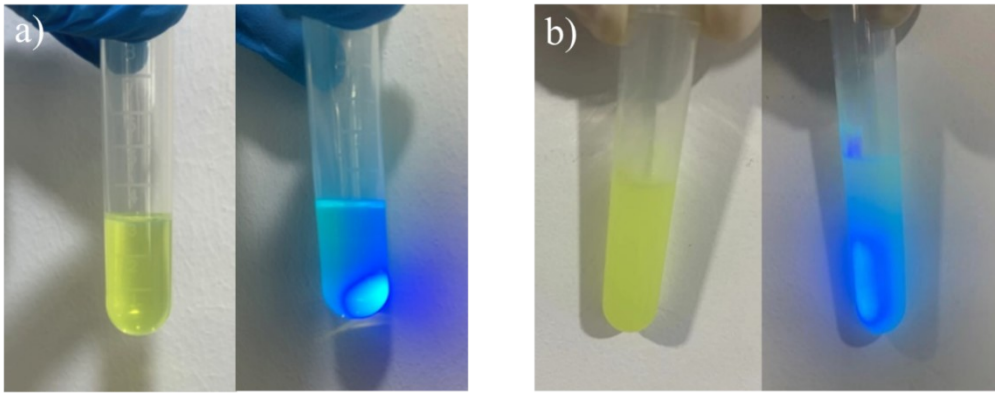

Figure S1 The photographic images of a) $CsPbBr_3$-OA nanosheets and b) $CsPbBr_3$ nanosheets dispersed in hexane under room light (left) and excitation using an ultraviolet lamp under room temperature (right).

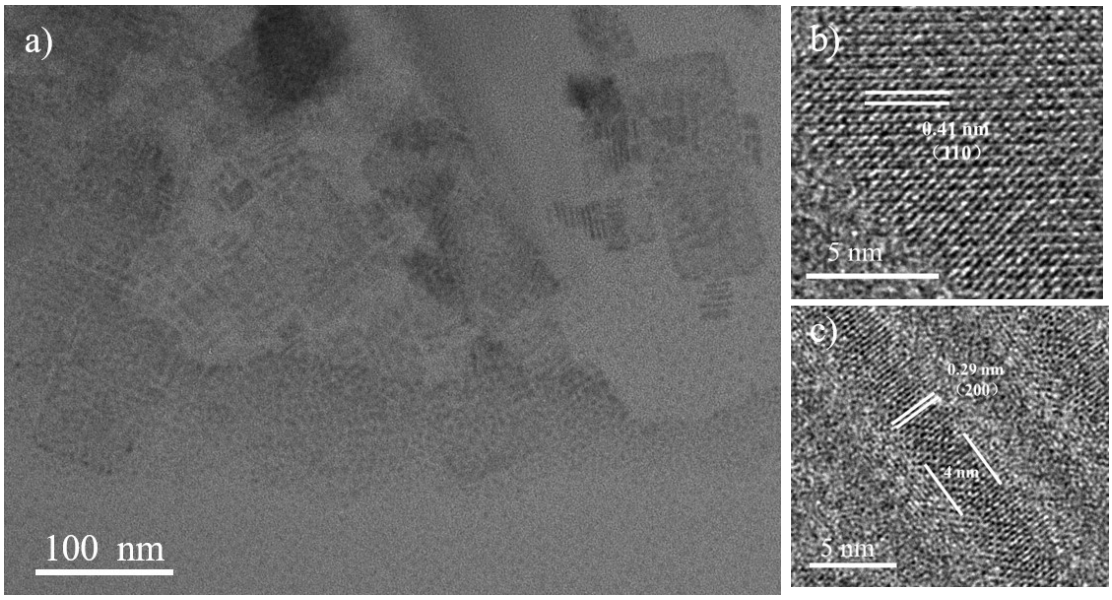

Figure S2 a) TEM image of $CsPbBr_3$-OA nanosheets. b-c) HRTEM images and lattice spacing of $CsPbBr_3$-OA nanosheets.

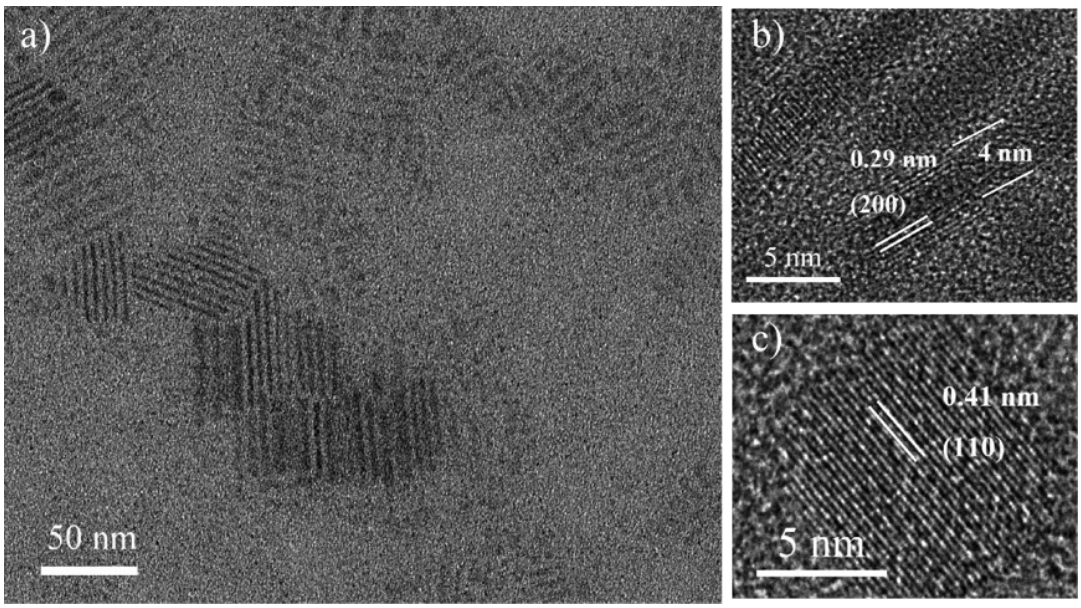

Figure S3 a) TEM image of $CsPbBr_3$ nanosheets. b-c) HRTEM images and lattice spacing of $CsPbBr_3$ nanosheets.

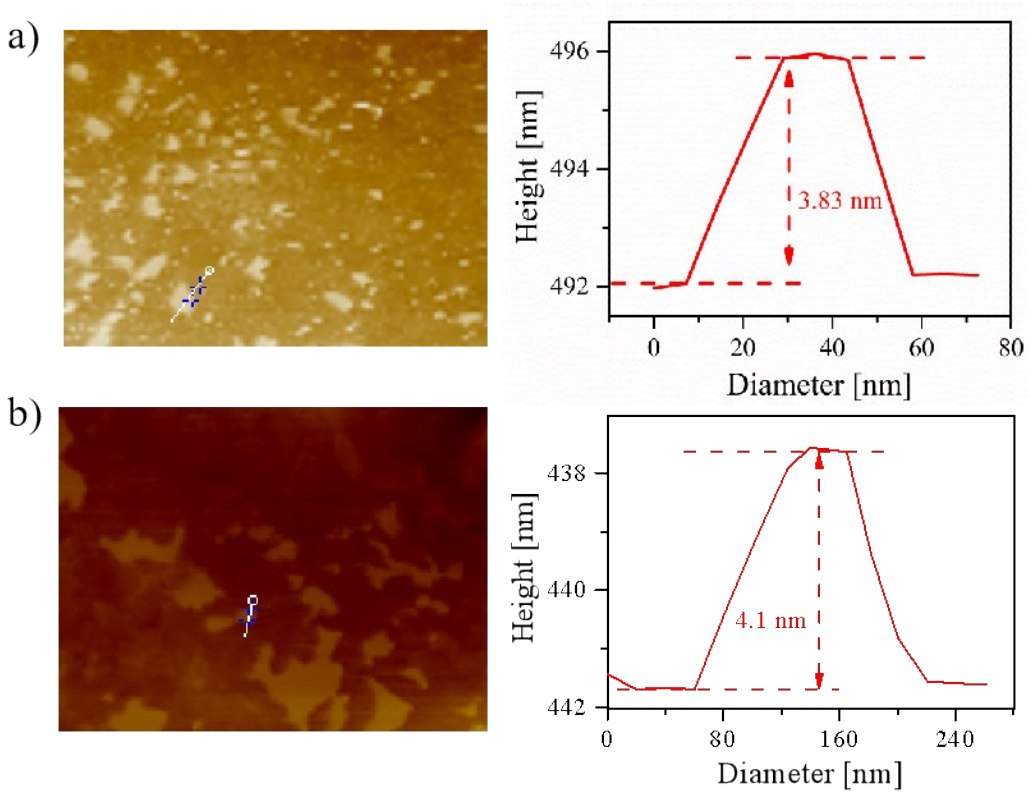

Figure S4 AFM images and corresponding height profiles of as prepared (a) $CsPbBr_3$ - OA nanosheets and (b) $CsPbBr_3$ nanosheets.

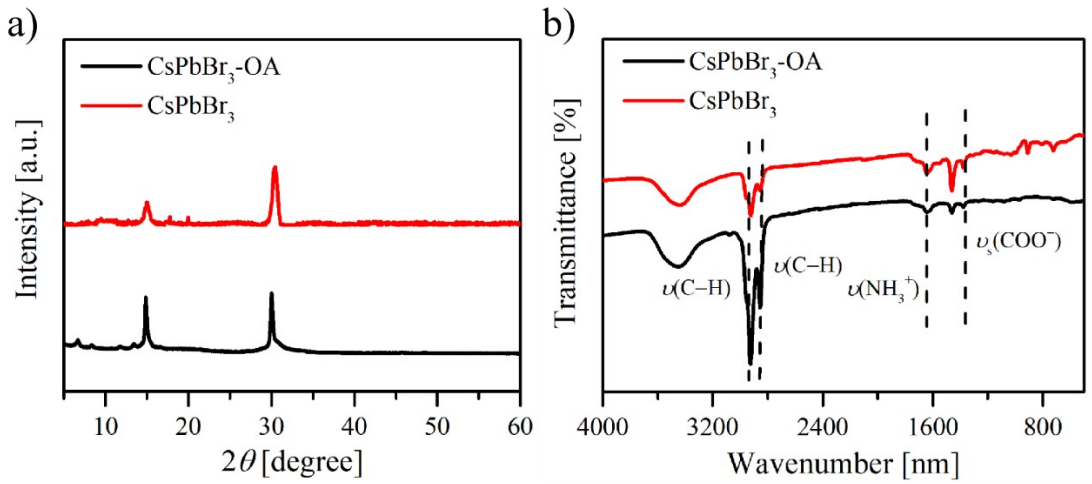

Figure S5 a) XRD patterns of $CsPbBr_3$-OA nanosheets and $CsPbBr_3$ nanosheets. b) IR spectrum of $CsPbBr_3$-OA nanosheets and $CsPbBr_3$ nanosheets.

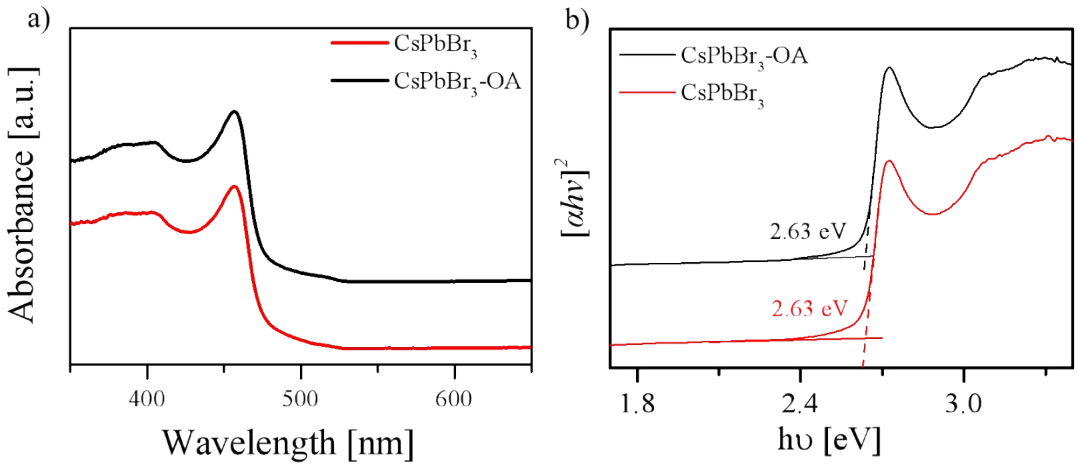

Figure S6 a) The UV-Vis absorption spectra of $CsPbBr_3$-OA nanosheets and $CsPbBr_3$ nanosheets. b) The Tanuc plots of $CsPbBr_3$-OA nanosheets and $CsPbBr_3$ nanosheets.

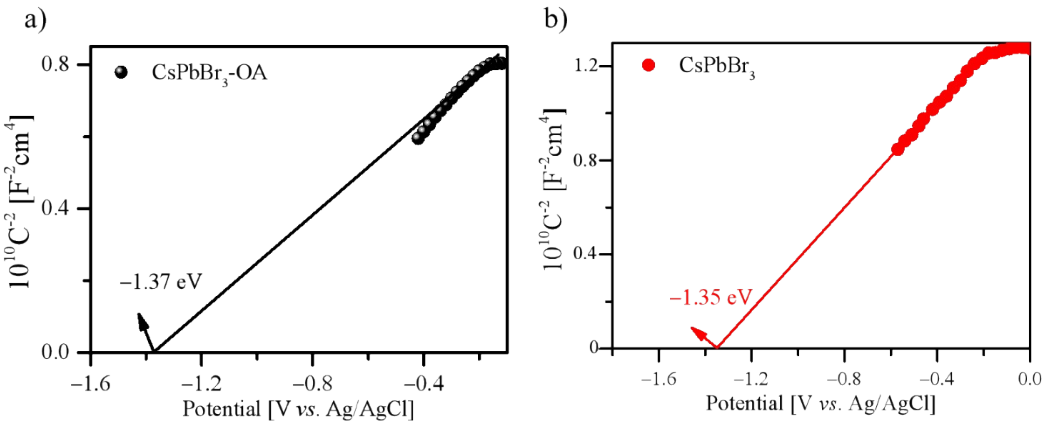

Figure S7 a) The UV-Vis absorption spectra of $CsPbBr_3$-OA nanosheets and $CsPbBr_3$ nanosheets. b) The Tanuc plots of $CsPbBr_3$-OA nanosheets and $CsPbBr_3$ nanosheets.

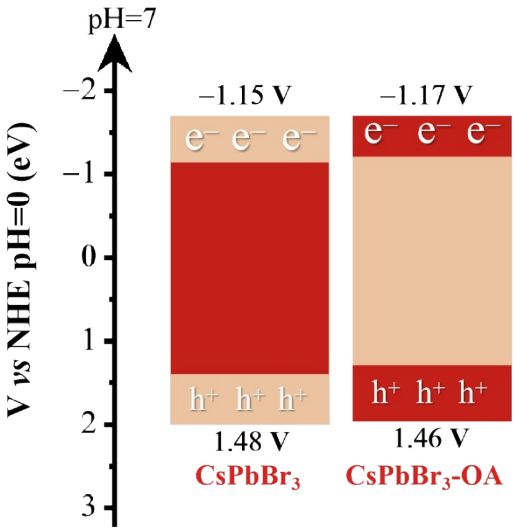

Figure S8 The band alignment of $CsPbBr_3$-OA nanosheets and $CsPbBr_3$ nanosheets.

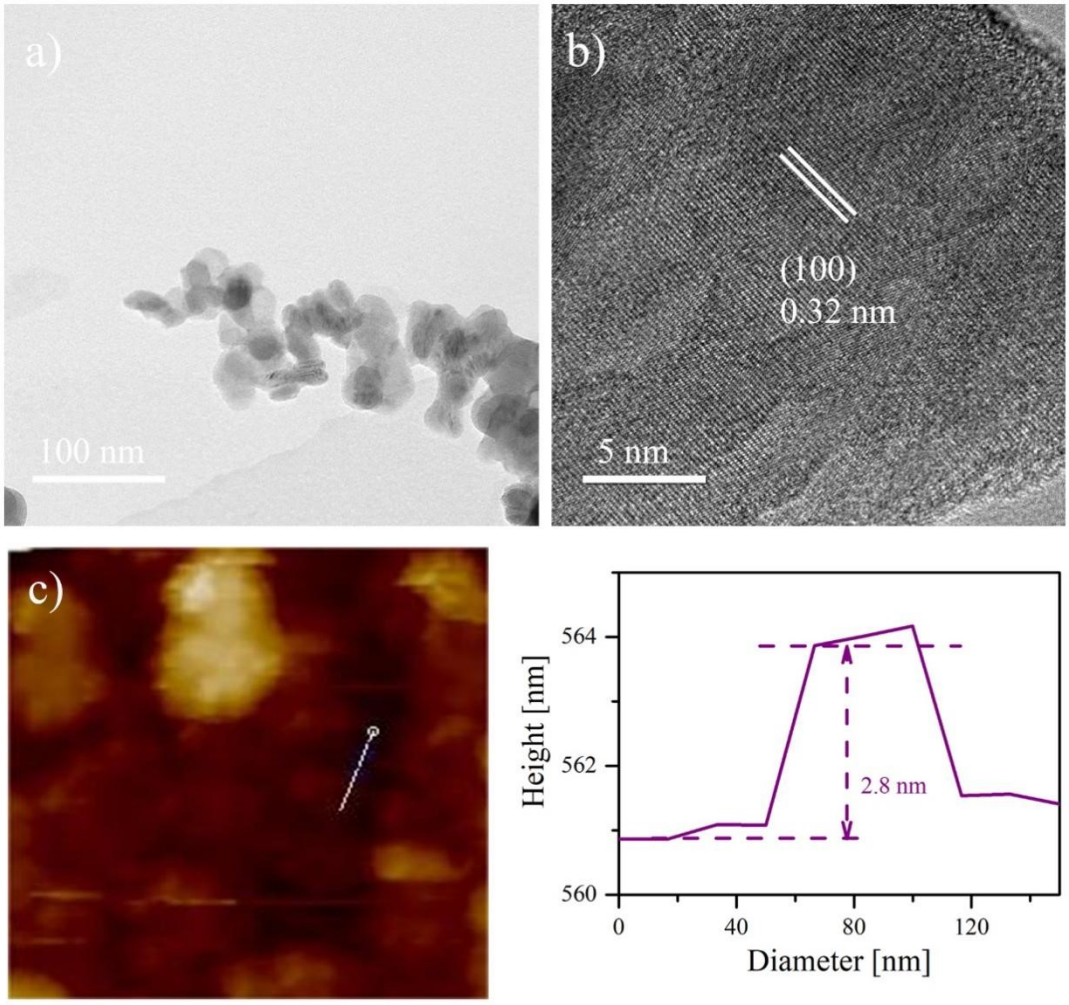

Figure S9 a) TEM, b) HRTEM images with lattice spacing of as prepared SnS_2 nanosheets. c) AFM image and corresponding height profiles of as preared SnS_2 nanosheets.

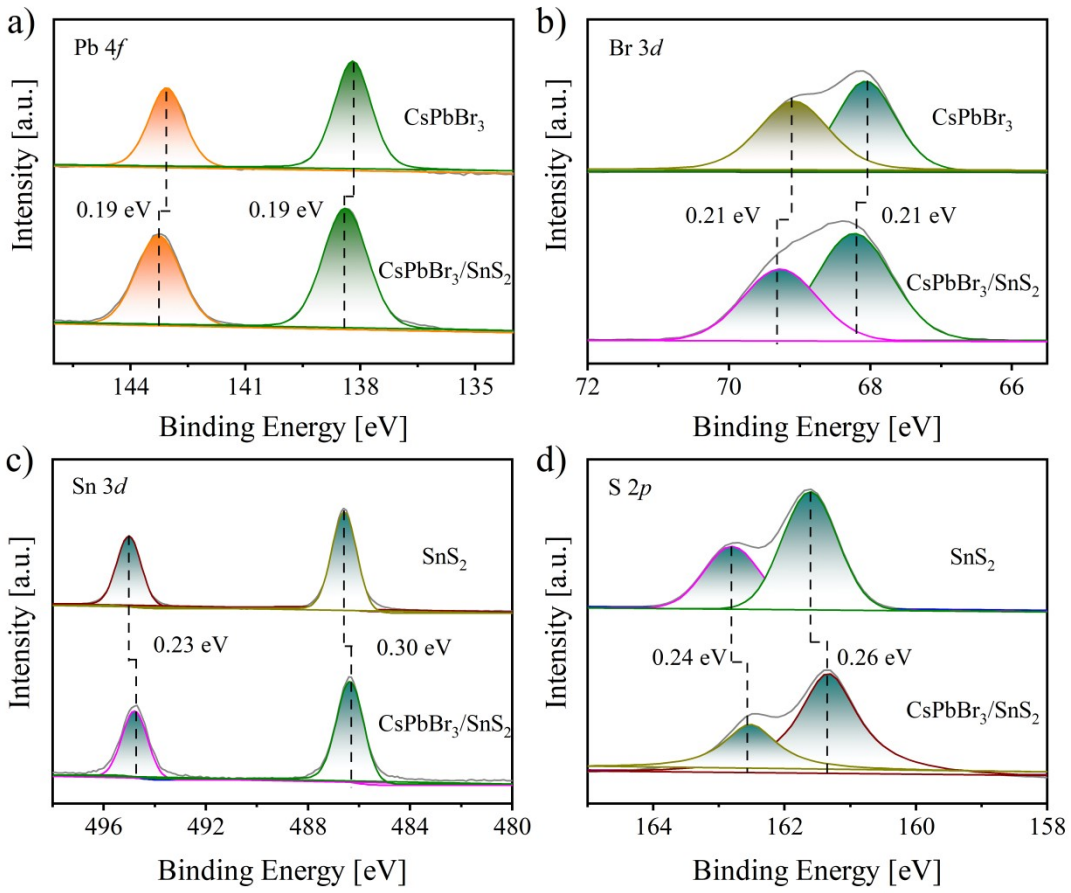

Figure S10 High-resolution XPS spectra of $CsPbBr_3/SnS_2$ composites in the dark (a) Pb 4*f*, (b) Br 3*d*, (c) Sn 3*d* and (d) S 2*p*.

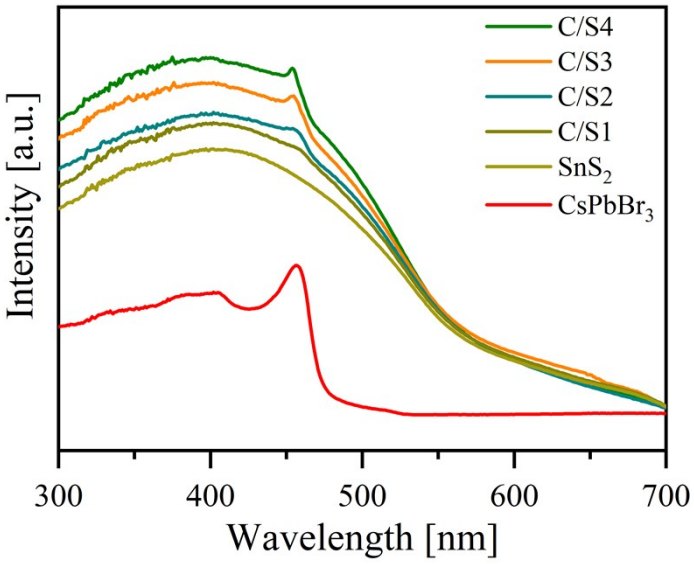

Figure S11 UV−Vis DRS spectra of S/C*x* heterojunctions.

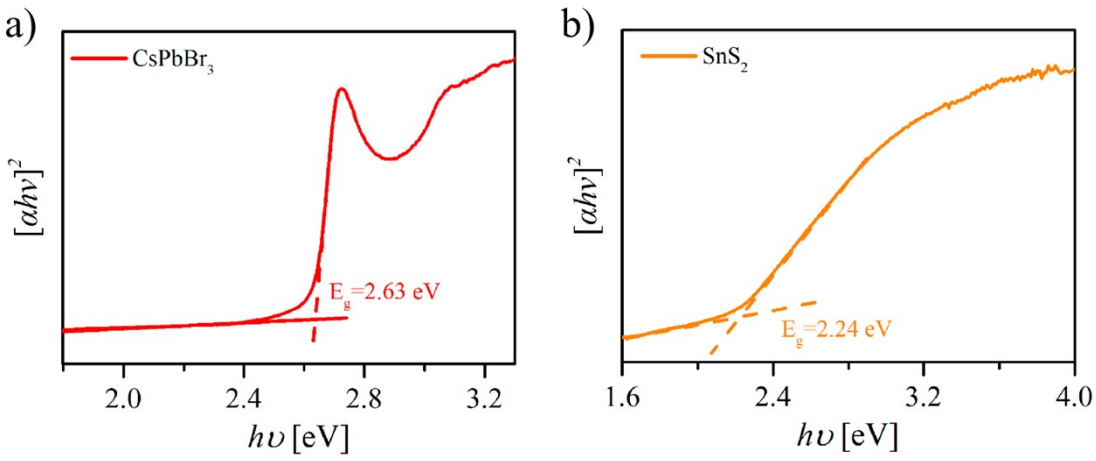

Figure S12 Tauc plots of $CsPbBr_3$ nanosheets and SnS_2 nanosheets.

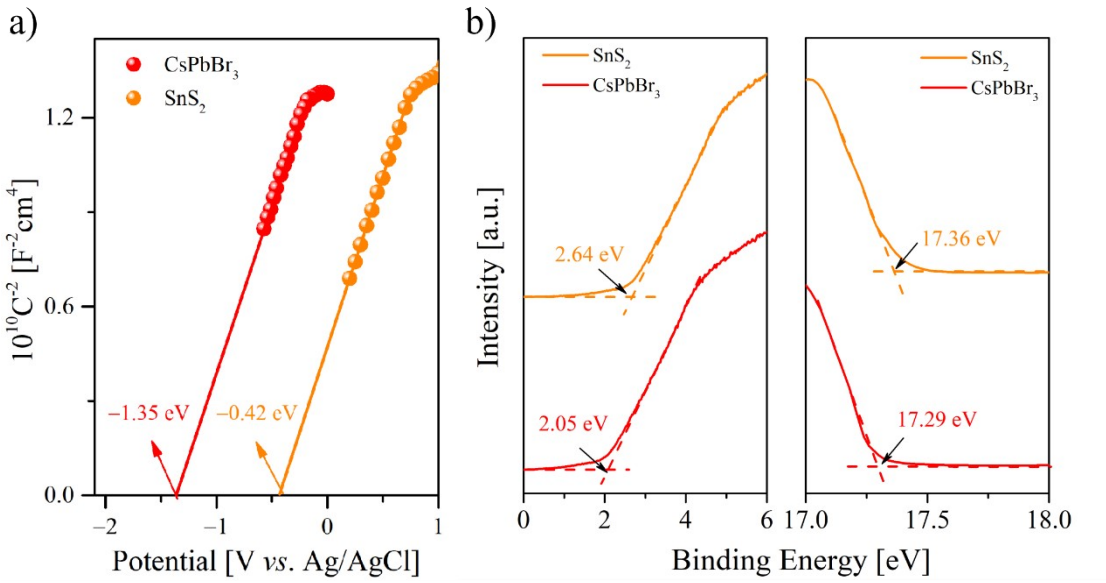

Figure S13 a) The Mott-Schottky plots and b) UPS spectras of SnS_2 nanosheets and $CsPbBr_3$ nanosheets.

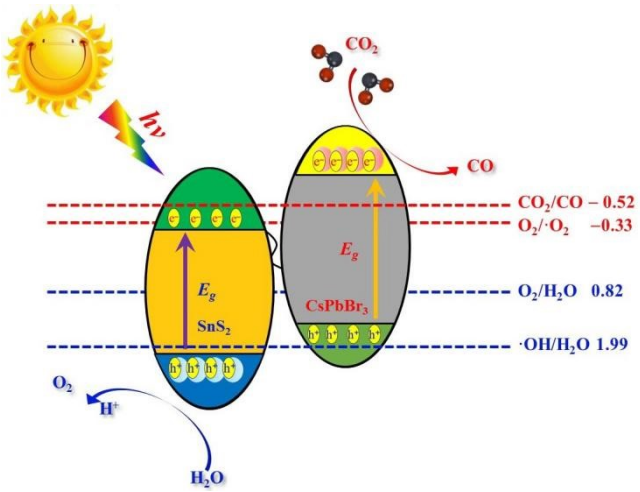

Figure S14 The band alignment of $CsPbBr_3$ nanosheets and SnS_2 nanosheets.

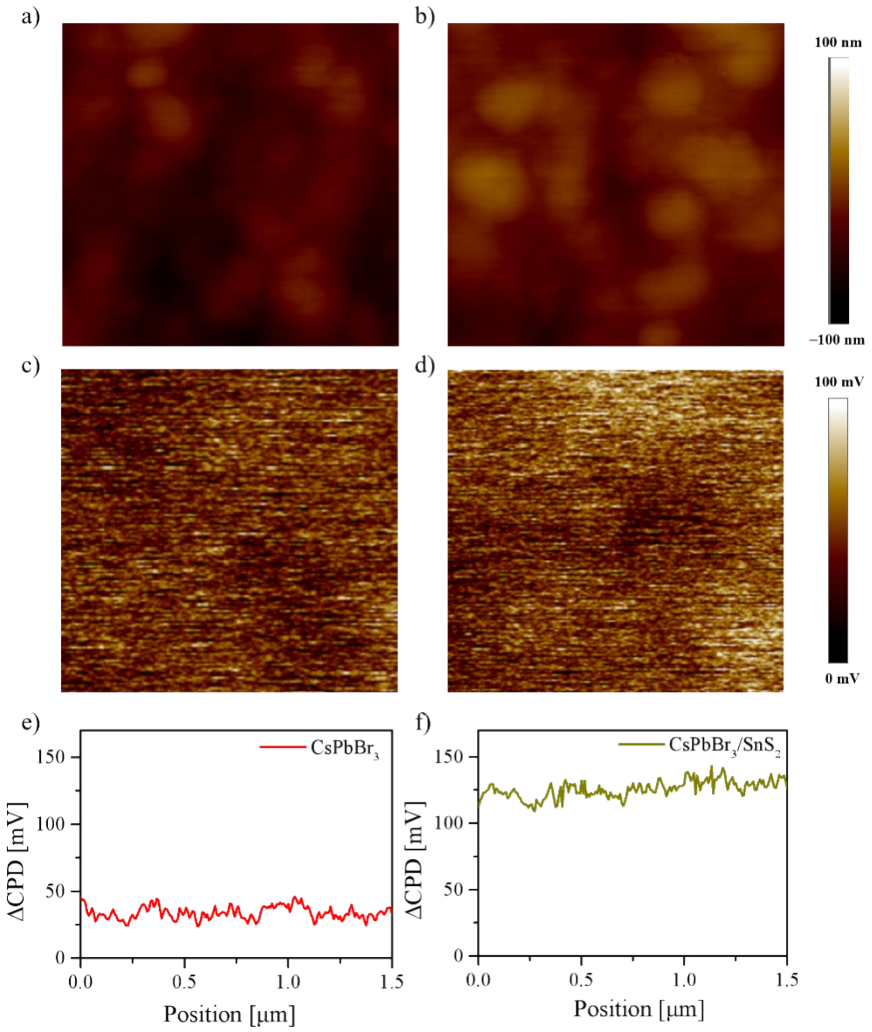

Figure S15 Height images of a) $CsPbBr_3$ and b) S/C2 heterojunctions. The differential surface photovoltage (SPV) images of c) $CsPbBr_3$ and d) S/C2 heterojunctions between potential images under illumination. Contact potential difference changes (ΔCPD) of e) $CsPbBr_3$ and f) S/C2 heterojunctions by subtracting the potential in the dark conditions from that under illumination.

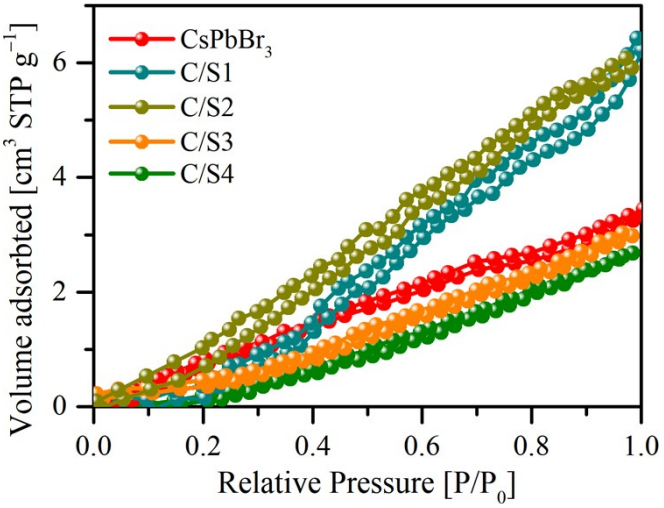

Figure S16 Carbon dioxide adsorption-desorption isotherm (BET) of $CsPbBr_3/SnS_2$ heterojunctions.

Table S1 Multi-exponential fitting parameters for the PL decays of $CsPbBr_3/SnS_2$ heterojunctions (Figure 3d). Excitation at 410 nm and detection at 460 nm.

Smaples	τ_1 [ns] (A_1)	τ_2 [ns] (A_2)	τ_3 [ns] (A_3)	τ_{Ave} [ns]
$CsPbBr_3$	0.77 (31.69%)	3.08 (46.16%)	9.56 (22.15%)	3.77
C/S1	0.48 (37.98%)	3.73 (37.51%)	25.38 (24.51%)	7.80
C/S2	1.91 (15.04%)	8.45 (42.54%)	36.43 (42.43%)	19.34
C/S3	0.79 (20.81%)	5.41 (41.64%)	32.88 (37.55%)	14.77
C/S4	1.11 (17.72%)	5.97 (47.75%)	28.11 (34.53%)	12.75

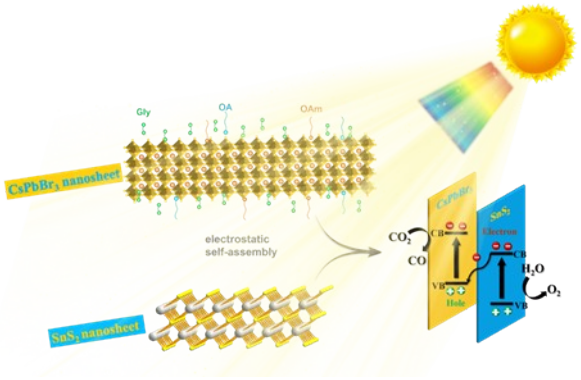

$CsPbBr_3/SnS_2$ Z-scheme heterojunctions were subtly constructed for visible-light-driven CO_2-to-CO conversion. This dual-nanosheet assembly is bonded via electrostatic attraction and exhibits excellent performance for CO_2 reduction to CO. The atomic-scale proximity in the 2D/2D architecture ensures efficient interfacial Z-scheme charge transfer.